ELSEVIER

Engineering Analysis with Boundary Elements 30 (2006) 671–686

ENGINEERING ANALYSIS with BOUNDARY ELEMENTS

www.elsevier.com/locate/enganabound

Two-dimensional velocity-vorticity based LES for the solution of natural convection in a differentially heated enclosure by wavelet transform based BEM and FEM

J. Ravnik*, L. Škerget, M. Hriberšek

Faculty of Mechanical Engineering, Institute of Power, Process and Environmental Engineering, University of Maribor, Smetanova 17, SI-2000 Maribor, Slovenia

Received 12 August 2005; accepted 28 February 2006
Available online 19 May 2006

Abstract

A wavelet transform based boundary element method (BEM) numerical scheme is proposed for the solution of the kinematics equation of the velocity-vorticity formulation of Navier–Stokes equations. FEM is used to solve the kinetics equations. The proposed numerical approach is used to perform two-dimensional vorticity transfer based large eddy simulation on grids with 10^5 nodes. Turbulent natural convection in a differentially heated enclosure of aspect ratio 4 for Rayleigh number values $Ra = 10^7 - 10^9$ is simulated. Unstable boundary layer leads to the formation of eddies in the downstream parts of both vertical walls. At the lowest Rayleigh number value an oscillatory flow regime is observed, while the flow becomes increasingly irregular, non-repeating, unsymmetric and chaotic at higher Rayleigh number values. The transition to turbulence is studied with time series plots, temperature–vorticity phase diagrams and with power spectra. The enclosure is found to be only partially turbulent, what is qualitatively shown with second order statistics—Reynolds stresses, turbulent kinetic energy, turbulent heat fluxes and temperature variance. Heat transfer is studied via the average Nusselt number value, its time series and its relationship to the Rayleigh number value.

PACS: 47.11.+j; 44.25.+f

Keywords: Boundary element method; Velocity-vorticity formulation; Discrete wavelet transform; Large eddy simulation; Natural convection

1. Introduction

Over the last few decades two-dimensional (2D) buoyancy driven flows have been investigated thoroughly by several authors. Besides the Rayleigh–Bernard type problems, enclosures heated from the side and insulated on the top and bottom were also of prime interest. Usually a rectangular domain is under consideration with different width to height ratios. Natural convection in a rectangular enclosure is present in many industrial applications, such as cooling of electronic circuitry, nuclear reactor insulation and ventilation of rooms.

A benchmark solution for 2D flow of Boussinesq fluid in a square differentially heated enclosure was presented by De Vahl Davies and Jones [1]. They used the stream function-vorticity formulation. Vierendeels et al. [2,3] used a multigrid method to obtain a solution of a compressible fluid in a square enclosure for Rayleigh numbers between $Ra = 10^2$ and 10^7. Škerget and Samec [4] confirmed these results using a compressible 2D boundary element method (BEM) formulation. Weisman et al. [5] studied the transition from steady to unsteady flow for compressible fluid in a 1:4 enclosure. They found that the transition occurs at $Ra \approx 2 \times 10^5$. Different geometrical arrangement may lead to an unsteady behaviour at intermediate Rayleigh number values, while steady behaviour was observed at high Rayleigh number values, as reported by Oosthuizen and Paul [6]. Ingber [7] used the vorticity

*Corresponding author.
E-mail addresses: jure.ravnik@uni-mb.si (J. Ravnik), leo@uni-mb.si (L. Škerget), matjaz.hribersek@uni-mb.si (M. Hriberšek).

0955-7997/$ - see front matter © 2006 Elsevier Ltd. All rights reserved.
doi:10.1016/j.enganabound.2006.02.008

formulation to solve both square and 1:8 differentially heated enclosures. Simulations as well as experiments of turbulent flow were also extensively investigated. Hsieh and Lien [8] considered numerical modelling of buoyancy-driven turbulent flows in enclosures using RANS approach. 2D DNS was performed by Xin and Le Quéré [9] for an enclosure with aspect ratio 4 up to Rayleigh number, based on the enclosure height, 10^{10} using expansions in series of Chebyshev polynomials. For aspect ratio larger than or equal to 4, the onset of unsteadiness is due to the instability of vertical boundary layers independently of the boundary conditions imposed on the horizontal walls. The onset of unsteadiness proceeds through a bifurcation which is of Hoph supercritical type. Salat et al. [10] compared the results of modelling turbulent natural convection at high Rayleigh number value between experimental data, 2D large eddy simulation (LES), 2D DNS and three-dimensional (3D) LES computations. They reported that only minor differences are observed between the 2D and 3D results and concluded that a 2D calculation could be used as a first approximation for general flow structure in cavities at Rayleigh number value about 10^{10}. Peng and Davidson [11] performed a LES study of turbulent buoyant flow in a 1:1 enclosure at $Ra = 1.59 \times 10^9$ using a dynamic Smagorinsky model as well as the classical Smagorinsky model with Van Driest damping.

In present work we have studied the onset of natural convection in a 1:4 differentially heated enclosure within the incompressible Boussinesq approximation. Transition from 2D steady laminar flow at enclosure width based Rayleigh number $Ra = 10^6$ via oscillatory motion at $Ra = 10^7$ to chaotic (turbulent) fluid flow at $Ra = 10^8, 10^9$ is simulated. The planar LES is used for velocity-vorticity formulation of the incompressible Navier–Stokes equations. The velocity-vorticity formulation of the Navier–Stokes equations in combination with the BEM is a promising concept for numerical solution of fluid flow problems. Solution of the flow kinematics equation is obtained by the BEM and provides boundary vorticity values, leading to a well posed vorticity transport equation. It is written in a form directly applicable for first kind boundary value problems. Velocity-vorticity LES has been investigated by Tenaud et al. [12] and Mansfield et al. [13], each having a different solution for boundary vorticity. We propose to use BEM because of its unique advantage for solving the boundary vorticity values directly.

For the solution of the domain values Škerget et al. [14] and Ramšak et al. [15] proposed a subdomain BEM technique. Although the subdomain technique results in sparse matrices, it still requires a considerable amount of computer memory and CPU time. These requirements were reduced by Žunič et al. [16], who proposed using FEM for the solution of the domain and was able to simulate 2D laminar flows in velocity-vorticity formulation. In order to be able to perform a LES simulation, we propose using a wavelet compression algorithm on fully populated matrices, resulting from the BEM calculation of boundary vorticities, to further decrease the computer memory and CPU time requirements of the coupled BEM–FEM algorithm. A discrete wavelet transform for vectors of arbitrary length, developed by Ravnik et al. [17], was used.

The paper is organized as follows: we first introduce the velocity-vorticity based LES. Section 3 explains the use of wavelet transformed BEM and FEM to perform LES. The numerical scheme, especially the wavelet compression algorithm, is thoroughly tested and validated on known benchmark and analytical examples in Section 4. Turbulent natural convection is simulated and the results are analysed and compared with other authors in Section 5. Finally, conclusions and remarks are given in the last section.

2. Velocity-vorticity based large eddy simulation

In this paper we assume an incompressible viscous Newtonian fluid with constant material properties: density $\rho = \rho_0$, viscosity $\nu = \nu_0$ and diffusivity $\alpha = \alpha_0$. The continuity equation (mass conservation law) within this approximation

$$\vec{\nabla} \cdot \vec{v} = 0 \tag{1}$$

requires the velocity field $\vec{v}$ to be solenoidal, i.e. divergence free. In order to write the Navier–Stokes equations buoyancy is modelled within the Boussinesq approximation. Density variations with temperature $\rho(T) = \rho_0[1 - \beta_T(T - T_0)]$ are considered only in the buoyancy term and defined by the thermal volume expansion coefficient β_T and the temperature difference. Since we are solving a coupled momentum–heat transport problem, the field functions were non-dimensionalized in the following manner: $\vec{v} \to \vec{v}/v_0$, $\vec{g} \to \vec{g}/g_0$, $\vec{r} \to \vec{r}/L$, $\vec{\omega} \to \vec{\omega}L/v_0$, $t \to v_0 t/L$, $T \to (T - T_0)/\Delta T$, $p \to p/p_0$, $v_0 = \alpha_0/L$, where p is the pressure, L the width of the enclosure and $\vec{\omega}$ the vorticity. With the above stated assumptions the momentum transport equation (momentum conservation law) in non-dimensional form reads as

$$\frac{\partial \vec{v}}{\partial t} + (\vec{v} \cdot \vec{\nabla})\vec{v} = -PrRa\ T\vec{g} - \frac{1}{Eu}\vec{\nabla}p + Pr\nabla^2\vec{v}, \tag{2}$$

with the Prandtl Pr, enclosure width based Rayleigh Ra and Euler Eu numbers defined as: $Pr = \nu_0/\alpha_0$, $Ra = g_0\beta_T\Delta T L^3/\nu_0\alpha_0$, $Eu = \rho_0 v_0^2/p_0$. We further assume that no internal energy sources are present in the fluid. We will not deal with high velocity flow of highly viscous fluid, hence we will neglect irreversible viscous dissipation. With this, the internal energy conservation law, written with temperature as the unknown variable, reads as

$$\frac{\partial T}{\partial t} + (\vec{v} \cdot \vec{\nabla})T = \nabla^2 T. \tag{3}$$

Since it is, due to limited computer power, not possible to solve the system of equations (1)–(3) for all scales of turbulent fluid motion, the LES approach was chosen. Assuming a high Reynolds number value and isotropic turbulence, Kolmogorov stated (pope [18]) stated that the

effect of small scales of turbulent motion is purely energetic. The small scales are responsible for dissipating the kinetic energy coming from disintegration of large eddies into internal energy of the fluid. By the low pass spatial filtering of the flow fields (velocity, vorticity, pressure, temperature), we eliminate the small scales of turbulent motion. On the other hand, we provide a computational mesh dense enough to capture all the physics of the filtered flow field. It has been shown [19], that the mesh element size is of the same order of magnitude as the filter width. For sharp spectral filter, both quantities are identical. The well established [18,19] LES approach is to filter the equations of continuity, momentum and heat transport and rewrite them in a form, having the same terms as the original equation with an additional term, describing the difference between the two equations, i.e. the dissipation effects. However, we will use velocity-vorticity based LES, where the vorticity transfer equation is filtered instead of the momentum transfer equation. Similarly to the Richardson's energy cascade, Taylor's [20] vorticity transfer hypothesis also proposes transfer of vorticity from the large scales towards the small scales and its dissipation by the small scales.

Let us first sketch the derivation of the velocity-vorticity formulation of the Navier–Stokes equations. Vorticity $\vec{\omega}$ is defined as the curl of the velocity $\vec{\omega} = \vec{\nabla} \times \vec{v}$. By definition vorticity must be divergence free $\vec{\nabla} \cdot \vec{\omega} = 0$. The continuity equation (1) is used to transform the vorticity definition into a kinematics equation. Applying the curl operator on the vorticity definition we obtain

$$\vec{\nabla} \times \vec{\omega} = \vec{\nabla} \times \vec{\nabla} \times \vec{v} = \vec{\nabla}(\vec{\nabla} \cdot \vec{v}) - \nabla^2 \vec{v} = -\nabla^2 \vec{v}$$
$$\Longrightarrow \nabla^2 \vec{v} + \vec{\nabla} \times \vec{\omega} = 0 \tag{4}$$

the kinematics equation, which relates the velocity and vorticity fields for every point in space and time. Both, the vorticity and velocity fields must be solenoidal, in order for this equation to be fulfilled.

The advection term in the momentum transport equation (2) may be rewritten in the following way: $(\vec{v} \cdot \vec{\nabla})\vec{v} = \frac{1}{2}\vec{\nabla} v^2 - \vec{v} \times \vec{\omega}$. Using this relationship and the expression for the Laplacian of velocity field (4) in Eq. (2) we find

$$\frac{\partial \vec{v}}{\partial t} + \frac{1}{2}\vec{\nabla} v^2 - \vec{v} \times \vec{\omega} = -PrRaT\vec{g} - \frac{1}{Eu}\vec{\nabla} p - Pr\vec{\nabla} \times \vec{\omega}. \tag{5}$$

We now apply the curl operator to Eq. (5) and thus eliminate both gradient terms. This eliminates pressure from the equation. Taking into account the definition of vorticity, we arrive at

$$\frac{\partial \vec{\omega}}{\partial t} - \vec{\nabla} \times (\vec{v} \times \vec{\omega}) = -PrRa\vec{\nabla} \times T\vec{g} - Pr\vec{\nabla} \times \vec{\nabla} \times \vec{\omega} \tag{6}$$

a form of vorticity transfer equation, which is appropriate for LES filtering. The filtering operation is defined by the following domain integral. If a field function is $u(\vec{x}, t)$, its filtered counterpart is

$$\bar{u}(\vec{x}, t) = \int_{\Omega} G(\vec{r}, \vec{x}) u(\vec{x} - \vec{r}, t)\, \mathrm{d}\vec{r}, \tag{7}$$

where the integral includes the whole flow domain Ω. We will use the sharp spectral filter kernel $G = \sin(\pi r/\Delta)/\pi r$, which is normed and homogenous, thus filtering and derivation commute with respect to time as well as with respect to coordinate. It is a low pass filter defined by its width Δ. It filters out all wave numbers above the critical wave number $k_c = \pi/\Delta$.

The application of the filter to Eq. (6) filters all field functions in linear terms. Special consideration is needed for the nonlinear term $\vec{\nabla} \times (\vec{v} \times \vec{\omega})$, which requires an introduction of a residual vorticity vector $\vec{\tau}^{\omega}$ that represents the difference of a filtered product and a product of filtered quantities $\vec{\tau}^{\omega} = \overline{\vec{v} \times \vec{\omega}} - \bar{\vec{v}} \times \bar{\vec{\omega}}$. The filtered Eq. (6) reads as

$$\frac{\partial \bar{\vec{\omega}}}{\partial t} - \vec{\nabla} \times (\bar{\vec{v}} \times \bar{\vec{\omega}}) = -PrRa\vec{\nabla} \times T\vec{g} - Pr\vec{\nabla} \times \vec{\nabla} \times \bar{\vec{\omega}} + \vec{\nabla} \times \vec{\tau}^{\omega}, \tag{8}$$

where we have, due to clarity of notation, omitted the bars indicating that all field functions have been filtered. By comparing non-filtered Eq. (6) with the filtered Eq. (8) we see, that the difference is only in the residual vorticity vector term $\vec{\nabla} \times \vec{\tau}^{\omega}$. Thus the residual vorticity vector $\vec{\tau}^{\omega}$ represents the dissipation of vorticity by the small scales according to the turbulent vorticity transfer theory of Taylor [20].

In order to derive the final form of the vorticity transport equation, the following two vector equations are needed, $\vec{\nabla} \times \vec{\nabla} \times \vec{\omega} = -\nabla^2 \vec{\omega}$ and $\vec{\nabla} \times (\vec{v} \times \vec{\omega}) = (\vec{\omega} \cdot \vec{\nabla})\vec{v} - (\vec{v} \cdot \vec{\nabla})\vec{\omega}$, where the solenoidality of velocity and vorticity fields were already taken into account. Using both in Eq. (8), the final form of the vorticity transport equation reads as

$$\frac{\partial \bar{\vec{\omega}}}{\partial t} + (\bar{\vec{v}} \cdot \vec{\nabla})\bar{\vec{\omega}} = (\bar{\vec{\omega}} \cdot \vec{\nabla})\bar{\vec{v}} + Pr\nabla^2 \bar{\vec{\omega}} - PrRa\vec{\nabla} \times T\vec{g} + \vec{\nabla} \times \vec{\tau}^{\omega}. \tag{9}$$

Equation (9) equates the Stokes rate of change of vorticity on the left-hand side with the vortex twisting and stretching term, the diffusion term, buoyancy and subgrid dissipation term on the right-hand side. The vortex twisting and stretching term $(\vec{\omega} \cdot \vec{\nabla})\vec{v}$ is responsible for the 3D character of turbulent flow. This term vanishes in cases of planar flows, where the vorticity vector is always perpendicular to the plane of motion.

The filtered form of the heat equation (3) is

$$\frac{\partial T}{\partial t} + (\bar{\vec{v}} \cdot \vec{\nabla})T = \nabla^2 T - \vec{\nabla} \cdot \vec{\tau}^{h}, \tag{10}$$

where the residual temperature vector $\vec{\tau}^{h}$ is defined as the difference between the filtered product of temperature and velocity field minus the product of filtered fields $\vec{\tau}^{h} = \overline{T\vec{v}} - \overline{T}\bar{\vec{v}}$.

Numerous LES studies used the Smagorinsky [21] and vorticity based [13] models for modelling the dissipative

effect of subgrid scales. Both types of models model the contribution of subgrid scales via the turbulent viscosity hypothesis. We are modelling the subgrid scales with analogy to molecular transfer of kinetic energy to heat; the process which is defined by viscosity. The residual heat vector is modelled using the gradient hypothesis. Here we are introducing a non-dimensional subgrid scale viscosity $v_{sgs} \rightarrow v_{sgs}/v_0 L = Pr(v_{sgs}/v_0)$ and subgrid diffusivity $\alpha_{sgs} = \alpha_{sgs}/\alpha_0$ by

$$\vec{\tau}^{\omega} = -v_{sgs}\vec{\nabla} \times \vec{\omega}, \quad \vec{\tau}^{h} = -\alpha_{sgs}\vec{\nabla}T. \tag{11}$$

When inserting the residual vorticity vector (11) into Eq. (9) we obtain

$$\frac{\partial \vec{\omega}}{\partial t} + (\vec{v}\cdot\vec{\nabla})\vec{\omega} = (\vec{\omega}\cdot\vec{\nabla})\vec{v} + Pr\nabla^2\vec{\omega} - PrRa\vec{\nabla} \times T\vec{g} - \vec{\nabla} \times (v_{sgs}\vec{\nabla} \times \vec{\omega}). \tag{12}$$

Further simplification is possible by using $\vec{\nabla} \times \vec{\nabla} \times \vec{\omega} = -\nabla^2\vec{\omega}$, the fact that the curl of a gradient is zero and the rule for a cross product of a product of a vector and scalar fields. When common terms are added we arrive at

$$\frac{\partial \vec{\omega}}{\partial t} + (\vec{v}\cdot\vec{\nabla})\vec{\omega} = (\vec{\omega}\cdot\vec{\nabla})\vec{v} + (Pr + v_{sgs})\nabla^2\vec{\omega} - PrRa\vec{\nabla} \times T\vec{g} + (\vec{\nabla} \times \vec{\omega}) \times \vec{\nabla}v_{sgs}. \tag{13}$$

Inserting the residual heat vector (11) into diffusion–advection equation for temperature (10) we obtain

$$\frac{\partial T}{\partial t} + (\vec{v}\cdot\vec{\nabla})T = (1 + \alpha_{sgs})\nabla^2 T + \vec{\nabla}T \cdot \vec{\nabla}\alpha_{sgs}. \tag{14}$$

Several models for the subgrid scale viscosity have been proposed. For vorticity transport equation (13) we decided to use the enstrophy based model given by Mansour [22,23]:

$$v_{sgs} = (C\Delta)^2\sqrt{\vec{\omega}\cdot\vec{\omega}}. \tag{15}$$

A sharp spectral filter is used; thus the filter width equals $\Delta = (\Delta_x\Delta_y\Delta_z)^{1/3}$. It is known [24] that turbulent oscillations die out in the vicinity of walls. Therefore, the residual vorticity vector (11) must also limit to zero when approaching a solid wall. Damping of the filter width is used to achieve zero residual tensor and vector at the wall [24]. We employed the Piomelli type damping d_P and Van Driest type damping d_{vd} to bring the subgrid scale viscosity to zero in the vicinity of solid walls:

$$d_P = \sqrt{1 - e^{[-y^+/25]^3}}, \quad d_{vd} = 1 - e^{[-y^+/25]},$$
$$v_{sgs} = (C\Delta d_P)^2\sqrt{\vec{\omega}\cdot\vec{\omega}}. \tag{16}$$

On the basis of experimental observations the turbulent viscosity of isotropic turbulence was found to be comparable with the turbulent diffusivity for the complete turbulent spectrum, their relationship being close to linear:

$$\alpha_{sgs} = \frac{1}{Pr_t}v_{sgs}, \tag{17}$$

where Pr_t is the empirically defined turbulent Prandtl number.

3. Coupled wavelet BEM–FEM solution algorithm

The solution of the vorticity-velocity based LES was obtained in planar geometry. Vorticity is a scalar quantity in 2D and does not fully describe turbulent motion (vortex twisting and stretching term vanishes in 2D). However, as it was reported by Salat et al. [10], for the case of turbulent natural convection in a differentially heated enclosure, the planar simulation can be used for the first approximation of the turbulent flow phenomena.

In planar geometry the kinematics equation (4) connects the velocity components v_x, v_y to the scalar vorticity field ω. The vortex twisting and stretching term of the vorticity transfer equation (13) vanishes. The planar LES vorticity transport equation is

$$\frac{\partial \omega}{\partial t} + (\vec{v}\cdot\vec{\nabla})\omega = (Pr + v_{sgs})\nabla^2\omega - PrRa\vec{\nabla} \times T\vec{g} + \vec{\nabla}\omega \cdot \vec{\nabla}v_{sgs}. \tag{18}$$

Our complete system of equations is thus made of: two scalar Poisson type kinematic equations for both velocity components equations (4) and of the diffusion–advection equations for temperature (14) and vorticity (18). Having the no-slip velocity boundary conditions on all walls, the wavelet based BEM is used to calculate boundary vorticities. For coarse grids, an explicit BEM calculation is used to obtain domain velocities. For fine grids storage requirements of BEM are too large, so instead the kinematics equations (4) are solved again by FEM to obtain domain velocities. With the new velocity field the temperature transport equation (14) is solved to obtain a new temperature field. Finally, the vorticity transport equation (18) is solved using the new boundary vorticities, domain velocities and temperatures. Both transport equations are solved by FEM. The procedure is repeated until convergence criteria is fulfilled (RMS difference between vorticity fields in subsequent iterations is used). In the following subsections the numerical procedure of wavelet BEM and FEM is explained.

3.1. Solution of the kinematics equation by wavelet based BEM

The kinematics equation (4) is an elliptic Poisson type equation. The basic BEM derivation [25] yields the following boundary-domain integral form

$$c(\xi)\vec{v}(\xi) + \int_\Gamma \vec{v}(\vec{n}\cdot\vec{\nabla})u^\star \,\mathrm{d}\Gamma = \int_\Gamma u^\star(\vec{n}\cdot\vec{\nabla})\vec{v}\,\mathrm{d}\Gamma + \int_\Omega (\vec{\nabla} \times \vec{\omega})u^\star \,\mathrm{d}\Omega, \quad \xi \in \Gamma, \tag{19}$$

where $u^\star$ is the fundamental solution of the Laplace equation ($u^\star = 1/4\pi r$ in 3D, $u^\star = (1/2\pi)\ln(1/r)$ in 2D), $\vec{n}$ the unit normal, ξ the source point and $c(\xi)$ the geometrical factor. The domain integral on the right-hand side of Eq. (19) is rewritten with the definition of a curl of a

product, i.e. $\vec{\nabla}\times(\vec{\omega}u^\star)=(\vec{\nabla}\times\vec{\omega})u^\star-\vec{\omega}\times\vec{\nabla}u^\star$ into

$$\int_\Omega(\vec{\nabla}\times\vec{\omega})u^\star\,\mathrm{d}\Omega=\int_\Omega(\vec{\nabla}\times(\vec{\omega}u^\star))\,\mathrm{d}\Omega+\int_\Omega(\vec{\omega}\times\vec{\nabla}u^\star)\,\mathrm{d}\Omega. \tag{20}$$

Using a derived form of the Gauss divergence clause, $\int_\Omega\vec{\nabla}\times\vec{F}\,\mathrm{d}\Omega=-\int_\Gamma\vec{F}\times\vec{n}\,\mathrm{d}\Gamma$, to change the first domain integral on the right-hand side of (20) into a boundary integral, yields

$$\int_\Omega(\vec{\nabla}\times\vec{\omega})u^\star\,\mathrm{d}\Omega=-\int_\Gamma(\vec{\omega}u^\star)\times\vec{n}\,\mathrm{d}\Gamma+\int_\Omega(\vec{\omega}\times\vec{\nabla}u^\star)\,\mathrm{d}\Omega. \tag{21}$$

Equation (21) is inserted into (19) and a new integral form of kinematics equation is obtained

$$c(\xi)\vec{v}(\xi)+\int_\Gamma\vec{v}(\vec{n}\cdot\vec{\nabla})u^\star\,\mathrm{d}\Gamma=\int_\Gamma u^\star\left\{(\vec{n}\cdot\vec{\nabla})\vec{v}-\vec{\omega}\times\vec{n}\right\}\mathrm{d}\Gamma+\int_\Omega(\vec{\omega}\times\vec{\nabla}u^\star)\,\mathrm{d}\Omega. \tag{22}$$

The term in curly brackets in the boundary integral on the right-hand side of Eq. (22) is for solenoidal fluid equal to $(\vec{n}\cdot\vec{\nabla})\vec{v}-\vec{\omega}\times\vec{n}=(\vec{n}\times\vec{\nabla})\times\vec{v}$. Using this relationship in Eq. (22) one can further rewrite the boundary integral as

$$\int_\Gamma u^\star(\vec{n}\times\vec{\nabla})\times\vec{v}\,\mathrm{d}\Gamma=\int_\Gamma(\vec{n}\times\vec{\nabla})\times(\vec{v}u^\star)\,\mathrm{d}\Gamma+\int_\Gamma\vec{v}\times(\vec{n}\times\vec{\nabla})u^\star\,\mathrm{d}\Gamma. \tag{23}$$

The first integral on the right-hand side of the above equation represents an integral over a closed surface of a tangential derivative of a vector function. For a continuous function, such integral is always equal to zero. When we apply the Gauss divergence clause on each component of the integral separately, we see that the terms in the resulting domain integrals cancel each other and thus the integral vanishes.

Inserting Eq. (23) into (22) we finally have an integral kinematics equation without derivatives of the velocity or vorticity fields:

$$c(\xi)\vec{v}(\xi)+\int_\Gamma\vec{v}(\vec{n}\cdot\vec{\nabla})u^\star\,\mathrm{d}\Gamma=\int_\Gamma\vec{v}\times(\vec{n}\times\vec{\nabla})u^\star\,\mathrm{d}\Gamma+\int_\Omega(\vec{\omega}\times\vec{\nabla}u^\star)\,\mathrm{d}\Omega. \tag{24}$$

In order to obtain discrete solution of the integral kinematics equation (24) the boundary Γ is divided into E boundary elements Γ_e and the domain Ω is divided into C domain cells Ω_c with $\Gamma\approx\sum_{e=1}^{E}\Gamma_e$ and $\Omega\approx\sum_{c=1}^{C}\Omega_c$. Eq. (24) may therefore be approximated by

$$c(\xi)\vec{v}(\xi)+\sum_{e=1}^{E}\int_{\Gamma_e}\vec{v}(\vec{n}\cdot\vec{\nabla})u^\star\,\mathrm{d}\Gamma=\sum_{e=1}^{E}\int_{\Gamma_e}\vec{v}\times(\vec{n}\times\vec{\nabla})u^\star\,\mathrm{d}\Gamma+\sum_{c=1}^{C}\int_{\Omega_c}(\vec{\omega}\times\vec{\nabla}u^\star)\,\mathrm{d}\Omega. \tag{25}$$

Within each boundary element and each internal cells the field functions are approximated by boundary N_i^b and domain N_i^d interpolation functions $\vec{v}=\sum_{i=1}^{n_b}\vec{v}^i N_i^b$ and $\vec{\omega}=\sum_{i=1}^{n_d}\vec{\omega}^i N_i^d$, where n_b and n_d are the number of nodes in a boundary element and in a domain cell. In this paper we used three node boundary elements and nine node Lagrange domain cells. Inserting approximations into Eq. (25) we have

$$c(\xi)\vec{v}(\xi)+\sum_{e=1}^{E}\sum_{i=1}^{n_b}\vec{v}^i\left(\int_{\Gamma_e}N_i^b(\vec{n}\cdot\vec{\nabla})u^\star\,\mathrm{d}\Gamma\right)=\sum_{e=1}^{E}\sum_{i=1}^{n_b}\vec{v}^i\times\left(\int_{\Gamma_e}N_i^b(\vec{n}\times\vec{\nabla})u^\star\,\mathrm{d}\Gamma\right)+\sum_{c=1}^{C}\sum_{i=1}^{n_d}\vec{\omega}^i\times\left(\int_{\Omega_c}N_i^d\vec{\nabla}u^\star\,\mathrm{d}\Omega\right). \tag{26}$$

There are three type of integrals in the above equation. In all, the integrand is a derivative of the fundamental solution multiplied by the interpolation function and the unit normal. The values of integrals depend solely on the mesh and the interpolation functions chosen, thus they can be calculated before starting the nonlinear iterative procedure. The integrals are traditionally named as $h_{i,e}$, $\vec{h}^{\star}_{i,e}$ and $\vec{d}_{i,c}$, respectively. With the new notation we may rewrite the discrete form of kinematics equation as

$$c(\xi)\vec{v}(\xi)+\sum_{e=1}^{E}\sum_{i=1}^{n_b}\vec{v}^i h_{i,e}=\sum_{e=1}^{E}\sum_{i=1}^{n_b}\vec{v}^i\vec{h}^{\star}_{i,e}+\sum_{c=1}^{C}\sum_{i=1}^{n_d}\vec{\omega}^i\times\vec{d}_{i,c}. \tag{27}$$

The boundary conditions of the numerical examples investigated in this work are prescribed velocity on the boundary. In order to obtain a non-singular system of equations for boundary vorticities from Eq. (27), one must use its tangential form [26], obtained by taking a cross product of Eq. (27) with the unit normal in the source point

$$c(\xi)\vec{n}(\xi)\times\vec{v}(\xi)+\vec{n}(\xi)\times\sum_{e=1}^{E}\sum_{i=1}^{n_b}\vec{v}^i h_{i,e}=\vec{n}(\xi)\times\sum_{e=1}^{E}\sum_{i=1}^{n_b}\vec{v}^i\times\vec{h}^{\star}_{i,e}+\vec{n}(\xi)\times\sum_{c=1}^{C}\sum_{i=1}^{n_d}\vec{\omega}^i\times\vec{d}_{i,c}. \tag{28}$$

We now define the planar geometry. The fluid flows in the $x-y$ plane, vorticity has only one non-zero component in the z direction. Since we are dealing with velocity on the boundary, it is convenient to introduce normal velocity $v_n = n_x v_x + n_y v_y$ and tangential velocity $v_t = n_x v_y - n_y v_x$ and treat vorticity as a scalar quantity $\vec{\omega} = \omega_z = \omega$. The integral vector $\vec{h}^t$ also has only one non-zero component and will be also treated as scalar h^t. When the cross products of Eq. (28) are calculated and the system of equations is simplified to planar geometry, we obtain a non-zero equation in z direction only:

$$c(\xi)v_t(\xi) + \sum_{e=1}^{E}\sum_{i=1}^{n_b} v_t^i h_{i,e} = -\sum_{e=1}^{E}\sum_{i=1}^{n_b} v_n^i h_{i,e}^t + \sum_{c=1}^{C}\sum_{i=1}^{n_d} \omega^i (n_x d_{i,c}^x + n_y d_{i,c}^y). \tag{29}$$

When the source point ξ is set in all boundary nodes, we obtain a system of equations relating $E \cdot n_b$ velocities normal to the boundary, $E \cdot n_b$ velocities tangential to the boundary and $C \cdot n_d$ vorticities in the domain and on the boundary. But, since we are using nine node Lagrange internal cells and three node bilinear boundary elements, the boundary nodes of each cell and element are shared by neighbouring elements and cells. The unknown velocities are represented by boundary vectors $v_t^i \to \{v_t\}$, $v_n^i \to \{v_n\}$. The vorticity is divided into a boundary vector $\omega_{i\in\Gamma}^i \to \{\omega^\Gamma\}$ and a domain vector $\omega_{i\in\Omega\setminus\Gamma}^i \to \{\omega^{\Omega\setminus\Gamma}\}$. The integrals are assembled into matrices accordingly. With the boundary vorticities as unknowns, the matrix-vector form of Eq. (29) is

$$[D^\Gamma]\{\omega^\Gamma\} = ([C]+[H])\{v_t\} + [H^t]\{v_n\} - [D^{\Omega\setminus\Gamma}]\{\omega^{\Omega\setminus\Gamma}\}. \tag{30}$$

The matrices $[D^\Gamma]$, $[C]$, $[H]$ and $[H^t]$ are square, fully populated and unsymmetric with the number of boundary nodes of rows and columns. Although full, the storage requirements for these matrices are not large, since the number of boundary nodes is very small compared to the number of domain nodes. On the other hand, the matrix $[D^{\Omega\setminus\Gamma}]$ is rectangular and also full and unsymmetric and has dimension of the number of boundary elements rows and the number of domain nodes columns. Storing this matrix in memory requires huge amount of onboard memory. To tackle this problem we employed a wavelet transform technique for rectangular matrices developed by Ravnik et al. [17]. The idea is to use wavelet compression only on the large matrix $[D^{\Omega\setminus\Gamma}]$ and leave all other matrices unchanged. The integrals needed to assemble the matrix $[D^{\Omega\setminus\Gamma}]$ are calculated by integrating a derivative of the Green's function across domain cells. Derivatives of the Green's function are singular at the source point and diminish quickly when going away from the source point. Thus we expect high integral values on the diagonal of the matrix and values close to zero away from the diagonal. The Haar wavelets are step functions of compact support and are therefore a good choice to describe quick changes in matrix elements value.

The wavelet transform is a linear process and may be described with a matrix product. Let W be the wavelet transform matrix, which can, via matrix vector multiplication, transform vectors of arbitrary length. The transform is based on Haar wavelets and the fast wavelet transform algorithm of Beylkin [27] combined with the algorithm, that enables transformation of vectors of arbitrary length introduced in [17]. An inverse wavelet transform can be obtained by multiplication with the transpose of the wavelet matrix W^{T}. The wavelet matrices W and W^{T} are not stored in memory but calculated on the fly since the location and values of non-zero elements is simple and known beforehand. Details on how to construct the matrix W can be found in [17].

We will calculate the matrix vector product $[D^{\Omega\setminus\Gamma}]\{\omega^{\Omega\setminus\Gamma}\}$ using a compressed matrix of integrals. In order for the compression to be efficient it is necessary to transform the row as well as columns of the matrix [27]. Since the product of wavelet matrix and its transpose is an identity, we may write

$$[D^{\Omega\setminus\Gamma}]\{\omega^{\Omega\setminus\Gamma}\} = W^{\mathrm{T}}(\underbrace{W[D^{\Omega\setminus\Gamma}]W^{\mathrm{T}}}_{[D_W^{\Omega\setminus\Gamma}]} W\{\omega^{\Omega\setminus\Gamma}\}). \tag{31}$$

The wavelet compressed matrix of integrals $[D_W^{\Omega\setminus\Gamma}] = W[D^{\Omega\setminus\Gamma}]W^{\mathrm{T}}$ is calculated only once, prior to the iterative process. Small (in absolute sense) elements of matrix $[D_W^{\Omega\setminus\Gamma}]$ may be zeroed without diminishing the accuracy of the matrix vector product in Eq. (31). The resulting sparse matrix is written in compressed row storage format to save computer memory. Regarding CPU time per iteration, the wavelet version of matrix vector product requires two additional sparse matrix vector products—wavelet transform of vorticity and inverse transform of the product. However, the matrix $[D_W^{\Omega\setminus\Gamma}]$ is sparse and compared to the full matrix vector product requires less CPU time. Efficiency of compression is tested and proved in the code validation section below.

The final wavelet BEM based discrete form of the kinematics equation for the calculation of boundary vorticity values is

$$[D^\Gamma]\{\omega^\Gamma\} = ([C]+[H])\{v_t\} + [H^t]\{v_n\} - W^{\mathrm{T}}\left([D_W^{\Omega\setminus\Gamma}]W\{\omega^{\Omega\setminus\Gamma}\}\right). \tag{32}$$

The solution of the system is obtained using a direct solver with LU decomposition.

3.2. Solution of the transport equations by FEM

The vorticity transport equation (18) and temperature transport equations (14) are both of the diffusion–advection type. Here we describe a FEM solution of a general form of equations. Let the unknown scalar field function (vorticity or temperature) be denoted by u. First of all the

partial time derivative has to be approximated by the following second order approximation

$$\frac{\partial u}{\partial t} \approx \frac{3u - 4u^n + u^{n-1}}{2\Delta t}, \tag{33}$$

where u is the field function to be calculated in the next time step, u^n the field function in the present time step, and u^{n-1} the previous time step field function. The time step size is Δt. Having the approximation of the time derivative in mind, one can state the general diffusion–advection equation in the form

$$\beta u + C_i \frac{\partial u}{\partial x_i} = D\nabla^2 u + \frac{\partial G_i}{\partial x_i} + M \tag{34}$$

with β, C_i, D, G_i and M functions of time and location. Einstein summation notation is employed with $i = 1, 2$. The classical Garlekin FEM procedure is employed. One calculates integrals over each domain cell Ω_c using interpolation functions N_k $(k = 1 \ldots n_d)$ as weighting functions:

$$\begin{aligned}\int_{\Omega_c} \beta N_k u \,\mathrm{d}\Omega + \int_{\Omega_c} C_i N_k \frac{\partial u}{\partial x_i}\,\mathrm{d}\Omega \\ = \int_{\Omega_c} D N_k \nabla^2 u \,\mathrm{d}\Omega + \int_{\Omega_c} N_k \frac{\partial G_i}{\partial x_i}\,\mathrm{d}\Omega \\ + \int_{\Omega_c} M N_k \,\mathrm{d}\Omega.\end{aligned} \tag{35}$$

The order of the diffusion term (the first term on the right-hand side of Eq. (35)) is decreased by the Green's first theorem:

$$\begin{aligned}\int_{\Omega_c} D N_k \nabla^2 u \,\mathrm{d}\Omega \\ = -\int_{\Omega_c} \vec{\nabla}(N_k D)\cdot\vec{\nabla}u \,\mathrm{d}\Omega + \int_{\Gamma_c} N_k D \vec{\nabla} u \cdot \mathrm{d}\vec{\Gamma} \\ = -\int_{\Omega_c} D\vec{\nabla}N_k \cdot \vec{\nabla}u \,\mathrm{d}\Omega - \int_{\Omega_c} N_k \vec{\nabla} D \cdot \vec{\nabla} u \,\mathrm{d}\Omega \\ + \int_{\Gamma_c} N_k D \vec{\nabla} u \cdot \mathrm{d}\vec{\Gamma}.\end{aligned} \tag{36}$$

Using Eq. (36) in Eq. (35) and summing up similar operators one obtains

$$\begin{aligned}\int_{\Omega_c} \beta N_k u \,\mathrm{d}\Omega + \int_{\Omega_c} \left[C_i + \frac{\partial D}{\partial x_i}\right] N_k \frac{\partial u}{\partial x_i}\,\mathrm{d}\Omega \\ = -\int_{\Omega_c} D \frac{\partial N_k}{\partial x_i}\frac{\partial u}{\partial x_i}\,\mathrm{d}\Omega + \int_{\Gamma_c} N_k D \vec{\nabla} u \cdot \mathrm{d}\vec{\Gamma} \\ + \int_{\Omega_c} N_k \frac{\partial G_i}{\partial x_i}\,\mathrm{d}\Omega + \int_{\Omega_c} M N_k \,\mathrm{d}\Omega.\end{aligned} \tag{37}$$

Field functions are approximated across the cells: $u = \sum_{l=1}^{n_d} N_l u_l$, $G_i = \sum_{l=1}^{n_d} N_l G_i^l$, $M = \sum_{l=1}^{n_d} N_l M_l$. We use $n_d = 9$ node biquadratic interpolation functions to interpolate the field function behaviour in the cells Ω_c. Using these approximations in Eq. (37) we get

$$\begin{aligned}\sum_{l=1}^{n_d} u_l \left\{\int_{\Omega_c} \beta N_k N_l \,\mathrm{d}\Omega\right\} + \sum_{l=1}^{n_d} u_l \left\{\int_{\Omega_c}\left[C_i + \frac{\partial D}{\partial x_i}\right] N_k \frac{\partial N_l}{\partial x_i}\,\mathrm{d}\Omega\right\} \\ = -\sum_{l=1}^{n_d} u_l \left\{\int_{\Omega_c} D\left(\frac{\partial N_k}{\partial x_i}\frac{\partial N_l}{\partial x_i}\right)\mathrm{d}\Omega\right\} \\ + \sum_{l=1}^{n_d} u_l \left\{\int_{\Gamma_c} N_k D \vec{\nabla} N_l \cdot \mathrm{d}\vec{\Gamma}\right\} \\ + \sum_{l=1}^{n_d} G_i^l \left\{\int_{\Omega_c} N_k \frac{\partial N_l}{\partial x_i}\,\mathrm{d}\Omega\right\} \\ + \sum_{l=1}^{n_d} M_l \left\{\int_{\Omega_c} N_k N_l \,\mathrm{d}\Omega\right\}.\end{aligned} \tag{38}$$

There are n_d $(k = 1 \ldots n_d)$ equations (38) for each internal cell. When we apply this procedure to all internal cells, we obtain $n_d \times n_{cells}$ equations. However, we have less unknowns, because nodes are shared by adjacent internal cells. We sum up the equations for each node and so the number of equations is reduced. During summing we see, that the contributions of boundary integrals cancel each other on cell boundaries that are not on the outside boundary of the whole domain. Hence, the boundary integrals must be calculated only for the external boundary and not for boundaries of each internal cell. Solution of the resulting linear system of equations is obtained by the BICGSTAB solver [28].

3.3. Solution of the kinematics equations for domain velocities

When the kinematics equations are solved by BEM all boundary velocities and vorticities are known. It is now possible to make an explicit BEM calculation to get the internal velocities. However, for this, a new integral matrix is needed, which is fully populated and unsymmetric and its size is number of all nodes squared. For the 10^5 node meshes considered in this paper this means storing 10^{10} double precision real numbers. This requires 74.5 GB of storage and is too large even if wavelet compression would be used.

Alternatively, we have decided to use FEM instead of the explicit calculation by BEM [16]. The kinematics equation (4) is of Poisson type and the BEM calculation provided the Dirichlet boundary conditions. The Poisson type equation is just a simplification of the general diffusion–advection equation (34) solved in the previous section. The coefficients of the v_x equation are $\beta = 0$, $C_x = C_y = 0$, $D = 1$, $G_x = 0$, $G_y = \omega$, $M = 0$ and v_y equation are $\beta = 0$, $C_x = C_y = 0$, $D = 1$, $G_x = -\omega$, $G_y = 0$, $M = 0$. The domain velocities are thus solved by FEM as a simplified case of the general diffusion–advection equation.

4. Code validation

Our primary concern was the accuracy of the wavelet based matrix vector product needed to solve the kinematics

equation. The matrix depends solely on the shape and distribution of boundary elements and domain cells in the mesh. We have prepared meshes and calculated matrices, which were later used to perform numerical simulations. In order to test the efficiency of the wavelet compression algorithm, we made matrix vector multiplication tests. We multiplied uncompressed and compressed versions of the matrix with random vectors and calculated residual error with

$$\varepsilon_{res} = \frac{\sum_i |[D^{\Omega\setminus\Gamma}]\{\omega\}_i - [D_W^{\Omega\setminus\Gamma}]\{\omega\}_i|}{\sum_i |[D^{\Omega\setminus\Gamma}]\{\omega\}_i|}. \tag{39}$$

The residual error ε_{res} was compared for different compression ratios and meshes. The meshes used in this paper are listed in Table 1. Results of random vector multiplication tests are presented in Fig. 1. We have observed that denser mesh enables higher compression ratio. Based on the results of the test we decided to use compression ratio of approximately 90%, so that the matrix vector multiplication error will be around $\varepsilon_{res} = 10^{-5}$ in the same order of magnitude as the tolerance of the solver of linear equations.

To further assure that the wavelet compression does not decrease the accuracy of our code we performed steady simulation of lid driven cavity numerical example. The top boundary of a square cavity has a unit horizontal velocity prescribed, while the other walls have a non-slip boundary condition. The results for $Re = 5000$ are shown in Fig. 2 and are in excellent agreement with benchmark velocity profiles of [29]. To include the energy equation into benchmarking, we have solved the steady natural convection of air problem in a 2D closed square cavity. The left wall is heated, the right wall cooled, both are kept at a constant temperature. The top and bottom walls are insulated, i.e. adiabatic. This test case has been studied by De Vahl Davies and Jones [1] using stream function—vorticity formulation of the governing equations. The Prandtl number was taken to be $Pr = 0.71$ and our calculations were performed at Rayleigh number values of $Ra = 10^3$, 10^4, 10^5. The resulting heat flux through the walls measured by the Nusselt number value is compared with the benchmark results in Table 2. Again, we can confirm that $\approx 90\%$ compression of the domain integrals matrix on a mesh with 10^5 nodes gives accurate results.

To test the accuracy of the time scheme we decided to solve the Taylor problem. Stability analysis of Couette flow between two cylinders showed the existence of Taylor vortices [20]. Periodic counter rotation vortices, which diminish with time due to viscosity are a solution to Navier–Stokes equations. In the domain $[0,1;0,1]$ the analytical velocity field is given by

$$\vec{v} = (-\cos(2\pi x)\sin(2\pi y)\,\mathrm{e}^{-(8\pi^2/Re)t}, \\ +\cos(2\pi y)\sin(2\pi x)\,\mathrm{e}^{-(8\pi^2/Re)t}) \tag{40}$$

while the vorticity field and the stream function are

$$\omega = 4\pi\cos(2\pi x)\cos(2\pi y)\,\mathrm{e}^{-(8\pi^2/Re)t}, \quad \psi = \frac{\omega}{8\pi^2}. \tag{41}$$

The example was studied at Reynolds number value $Re = 8\pi^2$. Non-dimensional time step was $\Delta t = 0.01$ and calculation was performed on *32x32r11* mesh. The results are compared with analytical values at $t = 0.5$ and 1 s in Table 3. Very good agreement is obtained.

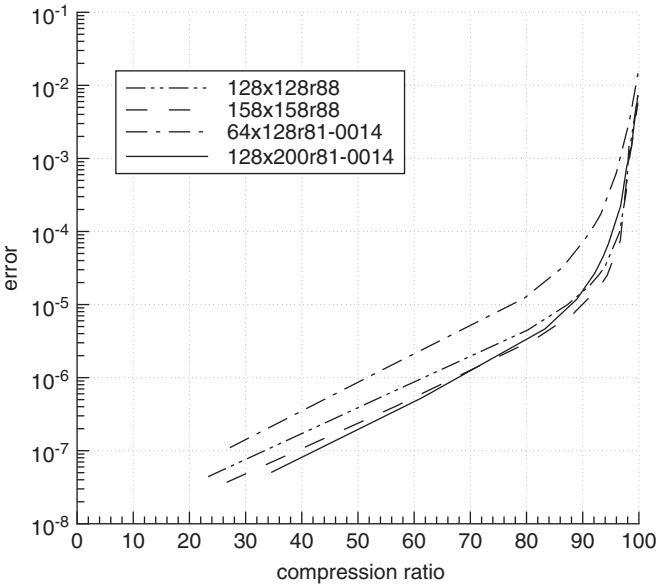

Fig. 1. Wavelet compression algorithm was tested on four meshes. Error of compressed matrix vector multiplication is presented.

Table 1
Description of meshes used in this paper

Mesh name	Number of elements	Number of bound. nodes	Number of nodes	Width:height ratio	Max:min el. width ratio	Max:min el. height ratio
32x32r11	1024	256	$65 \times 65 = 4225$	1:1	1	1
128x128r88	16384	1024	$257 \times 257 = 66049$	1:1	8	8
158x158r88	24964	1264	$317 \times 317 = 100489$	1:1	8	8
64x128r81-0014	8192	768	$129 \times 257 = 33153$	1:4	8	1
128x200r81-0014	25600	1321	$257 \times 401 = 103057$	1:4	8	1

The elements used are nine node bilinear rectangular Lagrange elements.

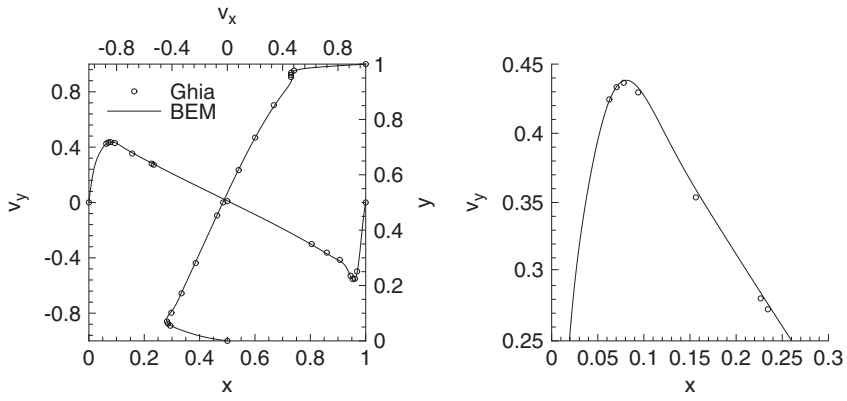

Fig. 2. Vertical and horizontal velocity profiles in the driven cavity test for $Re = 5000$ on a *158x158r88* mesh with 91.4% domain integrals matrix compression. The Ghia [29] benchmark velocity profiles are shown with circles.

Table 2
Comparison of simulated and benchmark [1] Nusselt number values for natural convection of air in a square cavity

	Compression	$Ra = 10^3$	$Ra = 10^4$	$Ra = 10^5$
Benchmark		1.118	2.243	4.519
158x158r88	0.917	1.1179	2.2448	4.5214
32x32r11	0.551	1.1198	2.2556	4.5810

Table 3
Comparison of simulated and analytical velocity and vorticity values for Taylor vortices at $Re = 8\pi^2$

	$\omega(1/2, 1/2)$		$v_x(1/2, 1/4)$		$v_y(3/4, 1/2)$	
	$t = 0.5$ s	$t = 1.0$ s	$t = 0.5$ s	$t = 1.0$ s	$t = 0.5$ s	$t = 1.0$ s
Simulation	7.6252	4.6266	0.6068	0.3681	0.6068	0.3681
Analytical	7.6219	4.6229	0.6065	0.3679	0.6065	0.3679
Analytical	$\frac{4\pi}{\sqrt{e}}$	$\frac{4\pi}{e}$	$\frac{1}{\sqrt{e}}$	$\frac{1}{e}$	$\frac{1}{\sqrt{e}}$	$\frac{1}{e}$

5. Onset of unsteady turbulent natural convection in an differentially heated enclosure

Natural convection of air ($Pr = 0.71$) in a differentially heated 1:4 enclosure is simulated with the above described planar vorticity based LES solved by wavelet BEM and FEM. The problem with initial and boundary conditions is presented in Fig. 3. The no slip boundary condition is prescribed on all walls. The left wall is heated and kept at constant temperature $T_h = 1$, while the right wall is cooled and kept at $T_c = 0$. The temperature was non-dimensionalized by $T_0 = T_h - T_c$. The top and bottom walls are adiabatic. All calculations were made on a *128x200r81-0014* mesh with 92.2% wavelet compression of the domain integrals matrix. Further data on the mesh may be found in Table 1 and in Fig. 3.

Three models were used to investigate the phenomena. First, we set the subgrid scale viscosity to zero and thus solve the problem directly, without a subgrid scale model, secondly LES was performed without damping (15) and thirdly LES with Piomelli and Van Driest damping (16).

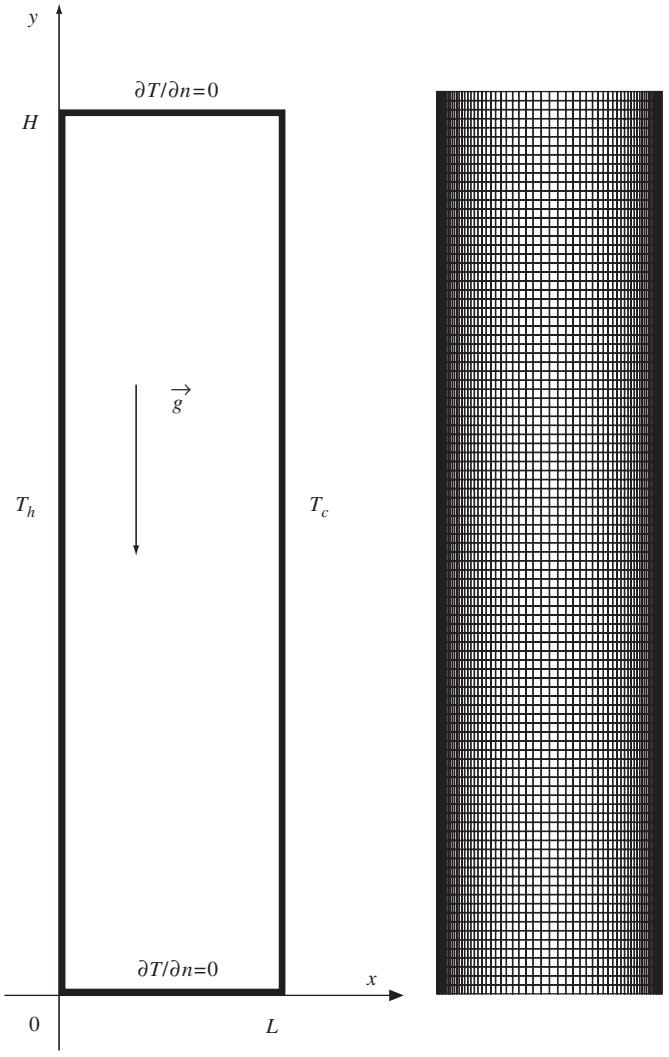

Fig. 3. Boundary and initial conditions for the simulation of natural convective flow in a rectangular enclosure with aspect ratio $L{:}H = 1{:}4$, $T_h = 1$ and $T_c = 0$. The presentation of the *128x200r81-0014* mesh. Only every fourth node is shown.

The LES constant was decreased from the theoretical value to $C = 0.1$ [19] and the turbulent Prandtl number was $Pr_t = 0.6$ [30]. The filter width was calculated as a square root of the cell size, $\Delta = \sqrt{\Delta_x \cdot \Delta_y}$.

The flow was simulated for enclosure width Rayleigh number $Ra = 10^6 - 10^9$. Please note, that the Rayleigh number used here is defined with respect to enclosure width, and is $4^3 = 64$ times smaller than the enclosure height based Ra used by some authors (e.g. [9,10]). Direct numerical simulation was used to simulate the problem at Rayleigh number $Ra = 10^6$. Steady state was reached regardless of the time step or mesh density. The smallest time step investigated was $\Delta t = 10^{-6}$. The resulting temperature (shown in Fig. 5) and velocity fields were used as the initial conditions for all higher Rayleigh number calculations.

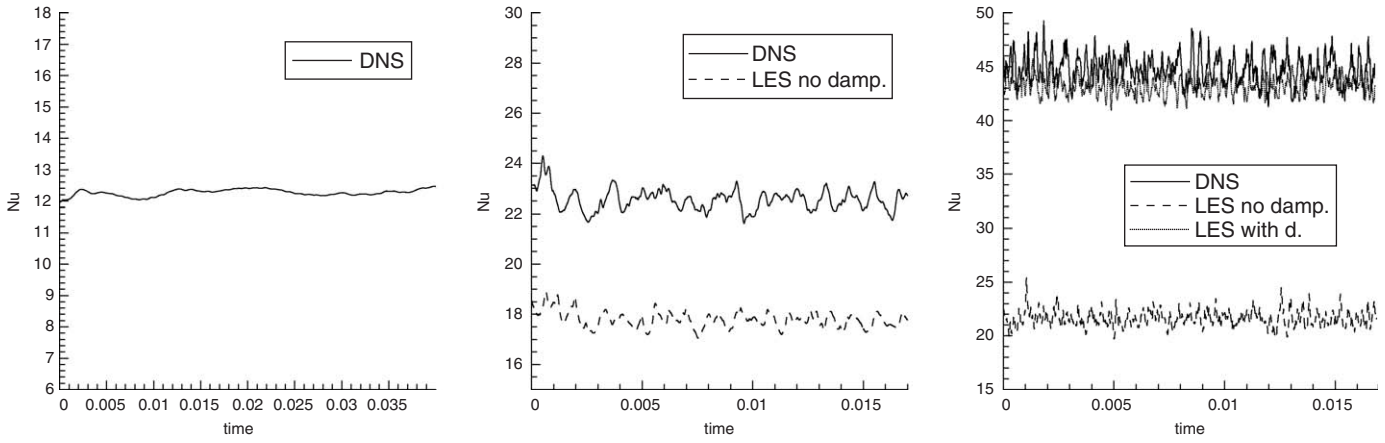

Fig. 4. Time traces of Nusselt number value for $Ra = 10^7$ (left), $Ra = 10^8$ (middle) and $Ra = 10^9$ (right).

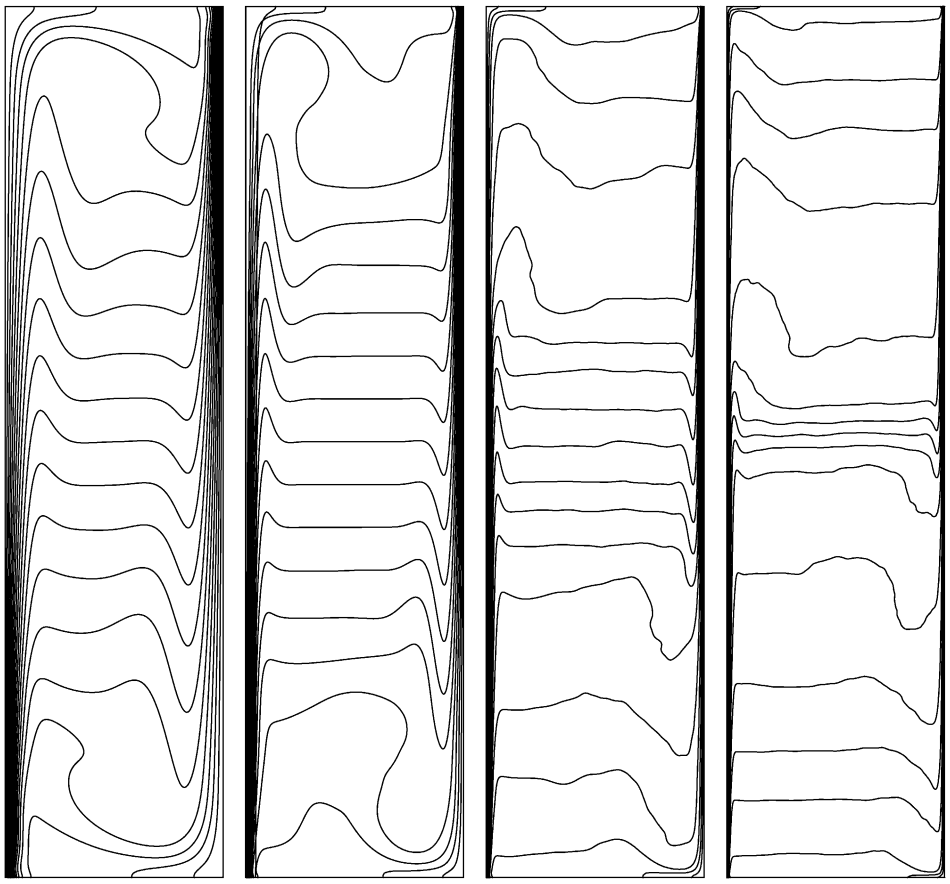

Fig. 5. Temperature fields (1(0.05)0): left to right: steady state at $Ra = 10^6$, time-average DNS results for $Ra = 10^7$, time-average LES with damping results for $Ra = 10^8$ and 10^9.

At Rayleigh number $Ra = 10^7$ we used a dimensionless time step of $\Delta t = 10^{-5}$, while at $Ra = 10^8$ and 10^9 we used $\Delta t = 10^{-6}$. In order for the flow field to reach self similar state we simulated 1000 time steps for $Ra = 10^7$ and 4000 time steps for $Ra = 10^8$ and 10^9 before starting analysing the results.

5.1. Flow dynamics

Steady state temperature field for $Ra = 10^6$ and averaged temperature fields of DNS at $Ra = 10^7$ and LES with Piomelli damping for $Ra = 10^8$ and 10^9 are shown in Fig. 5. While at $Ra = 10^6$ steady state is reached, at $Ra = 10^7$ the boundary layer becomes unstable and vortices are formed along the top of the hot wall and along the bottom part of the cold wall. Eddies are transported by convection up the hot wall and down the cold wall thus mixing the top and bottom parts of the enclosure. In the central part the temperature field is stratified and the flow is virtually steady. The whole flow field is oscillatory and symmetric. At $Ra = 10^8$ the eddies are formed more frequently. The formation takes place in the top half of the hot wall and in the bottom half of the cold wall. The stratified central core becomes smaller, but still exists. The flow field is no longer symmetric (although the initial $Ra = 10^6$ flow field was) length scales of the structures in the flow are becoming smaller. At $Ra = 10^9$ eddies are formed along the whole length of both vertical walls, most of them being formed at mid height. The central core is now thoroughly mixed and one can no longer speak of temperature stratification. The flow field includes eddies of various scales and is non-repeating, irregular and chaotic.

Average fields were used to draw temperature, vorticity and vertical velocity profiles in several heights in the enclosure (Fig. 6). We can readily observe the thinning of the boundary layer with the increasing Rayleigh number. The profiles show the vicinity of the hot wall, thus the lowest profiles are the thinnest, since vortices are not formed there. Vorticity increases dramatically at $Ra = 10^9$ which indicates the presence of small structures in the flow. The vertical velocity is largest in the bottom part of the hot boundary layer. Higher up the eddies are transported into the flow and thus disturb the boundary layer and decrease the vertical velocity. Instantaneous temperature fields are shown in Fig. 7 giving an impression of the wide variety of scales in the flow fields.

In the core area, the fluid is stratified. Average temperature fields were used to calculate the non-dimensional stratification parameter, S_p, given by $S_p = \partial T/\partial y|_{x=L/2,y=H/2}$. For $Ra = 10^7$ we obtained $S_p = 0.25$, for $Ra = 10^8$, $S_p = 0.30$ and for $Ra = 10^9$, $S_p = 0.77$. Tian and Karayiannis [31] reported $S_p = 0.5$ for $Ra = 1.58 \times 10^9$ in a square enclosure, while Xin and Le Quéré [9] reported S_p around 1 for $Ra = 10^9 - 10^{10}$.

5.2. Heat transfer

The heat transfer through the walls is represented by the average Nusselt number value, defined for our geometry by $Nu = 1/H \int_0^H (\partial T/\partial x)\,\mathrm{d}y$. The Nusselt number values versus time graphs are shown in (Fig. 4). The average values are compared with benchmark results of Xin and Le Quéré [9] in Table 4. The ratios $Nu/Ra^{1/4}$ and $Nu/Ra^{1/3}$ are found to be approximately constant. The average values and ratios are in excellent agreement with the benchmark for our simulation without a subgrid scale model ($C = 0$) at $Ra = 10^7$ and LES with damping simulation for $Ra = 10^8 - 10^9$. The subgrid scale viscosity in the LES without damping model does not tend to zero in the vicinity of the walls, thus the resulting boundary layer was thicker and the heat transfer lower. The fluid motion is oscillatory at $Ra = 10^7$ thus the direct simulation captures all the physics, since the subgrid scales do not exist at such low Rayleigh number. At $Ra = 10^8$ the damped LES model is virtually identical with the $C = 0$ simulation, while the non-damped LES results in lower heat transfer. The turbulence level at this Rayleigh number is still very low. Comparing the LES calculation with and without damping at $Ra = 10^9$ one observes that the difference becomes severe. The non-damped LES predicts lower heat transfer by half on order of magnitude. At $Ra = 10^9$ a comparison has been made between Piomelli and Van Driest damped LES. Both datasets were qualitatively equal, Van Driest simulation giving the average Nusselt number slightly closer to the benchmark (Table 4).

In the downstream part of the vertical boundary layers the formation of eddies results in local thickening or thinning of the thermal boundary layer. Thus the majority of heat transfer occurs in the upstream parts where the boundary layers are stable and thin.

5.3. Analysis of transition from oscillatory to chaotic low turbulent flow regime

In order to quantify the transition from steady fluid flow at $Ra = 10^6$ through the oscillatory phase observed at $Ra = 10^7$ to chaotic flow regime at $Ra = 10^8$ we first plotted the temperature versus time graphs. Fig. 8 shows the oscillatory nature of temperature versus time at $Ra = 10^7$, while the $Ra = 10^8$ and 10^9 graphs show a more non-repeating, irregular and chaotic character.

The transition from oscillatory to chaotic fluid motion can also be observed in temperature–vorticity phase portraits. The phase portraits were constructed from temperature versus time and vorticity versus time data from locations A = (0.0011, 3.5) and B = (0.0301, 3.5) and are shown in Fig. 9. Plotting both quantities as phase variables over a significant length of time, after the transients had decayed away, enables us to examine the topological structure of the attractor onto which the trajectory evolves at long-times [32]. The $Ra = 10^7$ phase portrait encompasses a small elliptical area—therefore the vorticity and temperature in this point are strongly correlated. The motion of the fluid is oscillatory, chaotic behaviour is not observed. The $Ra = 10^8$ phase portrait encompasses a distinctly larger $T - \omega$ area and has no

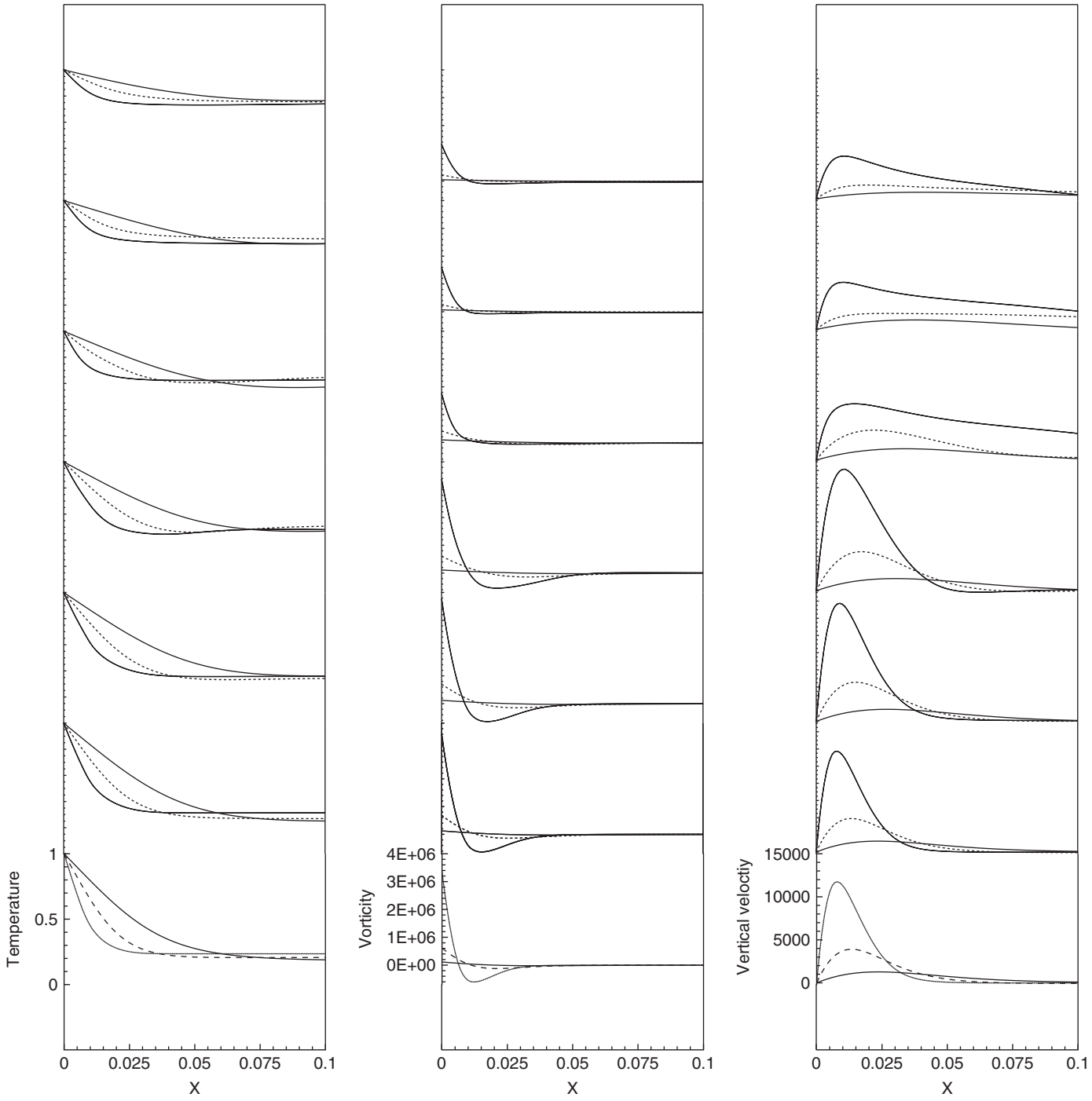

Fig. 6. Temperature, vorticity and vertical velocity profiles at $y = 0.5, 1.0, 1.5, 2.0, 2.5, 3.0, 3.5$ for the 10% of the cavity by the hot wall. Profiles for $Ra = 10^7$ are shown with solid line, $Ra = 10^8$ with dashed line and $Ra = 10^9$ with dotted line.

regular shape. Although some correlation between temperature and vorticity exists, the motion is becoming increasingly irregular and chaotic. Looking at the $Ra = 10^9$ phase portraits we see that it encompasses an even larger $T - \omega$ area. Although location A is very close to the hot wall with fixed temperature, we can observe considerably lower temperatures, which account for the increased heat transfer at this Rayleigh number.

Another proof of the transition from oscillatory to chaotic motion is provided by means of power spectrum plots. The power spectrum of the temperature time series at locations A and B was calculated with the discrete Fourier transform. The spectra are shown in Fig. 10. We are able to examine the frequencies of oscillations, and also the emergence of broad-band noise in the dynamics that occurs in chaotic flows. The dominant oscillatory

frequency, with which the eddies are formed at $Ra = 10^7$ is clearly visible. Comparing the $Ra = 10^7$ through $Ra = 10^9$ spectra one can observe the large increase of high frequency components with the increasing Rayleigh number. Besides the large structures the flow at higher Rayleigh numbers includes also smaller structures, thus the temperature changes occur in a wider frequency band.

5.4. Turbulent statistics

Second order statistics have been computed for the two highest Rayleigh number datasets. Since our simulations are 2D and the flow is not fully turbulent, the results in this section are presented for qualitative analysis only. Fig. 11 shows Reynolds stresses $\overline{v'_x v'_x}$, $\overline{v'_x v'_y}$, $\overline{v'_y v'_y}$, turbulent kinetic energy $k = \frac{1}{2}\overline{v'_i v'_i}$, turbulent heat fluxes $\overline{v'_x T'}$, $\overline{v'_y T}$ and temperature variance $\overline{T'T'}$ for $Ra = 10^8$ and 10^9. At $Ra = 10^8$ the plots show that these turbulent fluctuations dominate only in the downstream part of the vertical boundary layer, while the upstream part and a large part of the core remains laminar. This is consistent with the DNS results of Xin et al. [9], who considered the same problem. For the highest Rayleigh number, $Ra = 10^9$, the maximum fluctuations can be found in the vertical boundary layers in the middle of the enclosure. There, most of the eddies are formed. They are transported downstream and towards the centre of the enclosure. With increasing Rayleigh number value the maxima of turbulent kinetic energy moves upstream; it is well out of the vertical boundary layers.

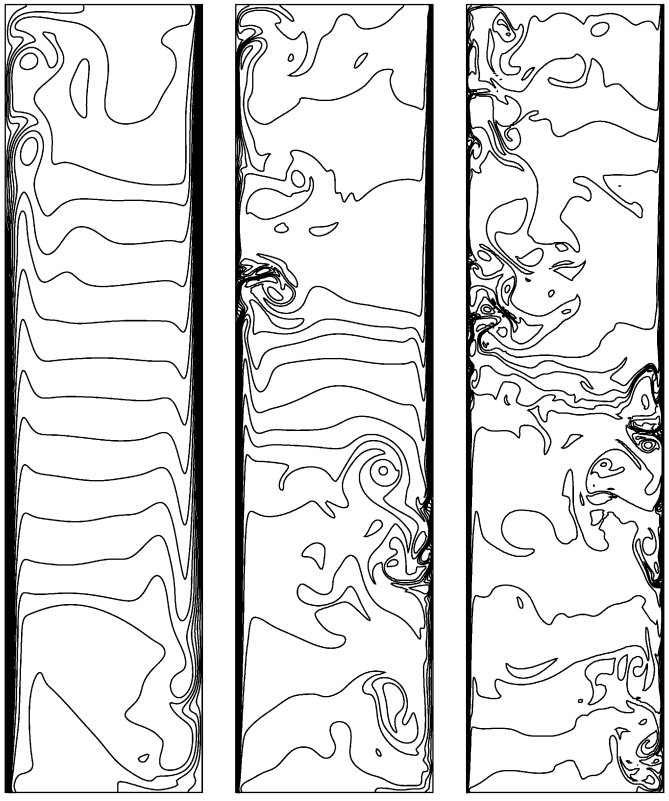

Fig. 7. Temperature fields (1(0.05)0): left to right: instantaneous DNS results for $Ra = 10^7$ ($t = 0.03$), LES with damping results for $Ra = 10^8$ ($t = 0.016$) and $Ra = 10^9$ ($t = 0.016$).

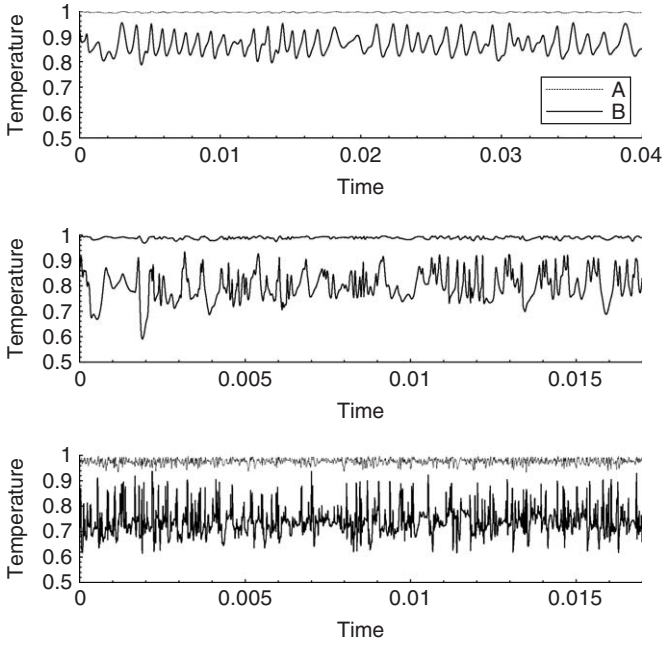

Fig. 8. Time traces of temperature for $Ra = 10^7$ (top), $Ra = 10^8$ (middle) and $Ra = 10^9$ (bottom). Temperature at location A = (0.0011, 3.5) and B = (0.0301, 3.5) is presented.

Table 4
Average Nusselt number Nu and correlation comparison with benchmark DNS results of Xin et al. [9]

Ra	Nu				$Nu/Ra^{1/4}$		$Nu/Ra^{1/3}$	
	$C = 0$	LES_p	LES_{vd}	Xin [9]	Present	Xin [9]	Present	Xin [9]
10^7	12.27			12.3	0.2181	0.2185	0.0569	0.0571
3.125×10^7		16.91^+		16.62		0.2227		0.0528
10^8	22.5	22.5		22.56^*	0.2256		0.0486	
1.56×10^8		25.57^+		25.25		0.2256		0.0469
10^9	44.77	43.25	43.67	43.63^*	0.2432		0.0433	

For the highest Rayleigh number Piomelli damped (LES_p) as well as Van Driest damped (LES_{vd}) results are presented. (*) For Nu at $Ra = 10^8$ and 10^9 Xin's values were predicted using their $Nu/Ra^{1/4}$ relationship. (+) Using present $Nu/Ra^{1/4}$ relationship Nu was predicted for $Ra = 3.125 \times 10^7$ and 1.56×10^8.

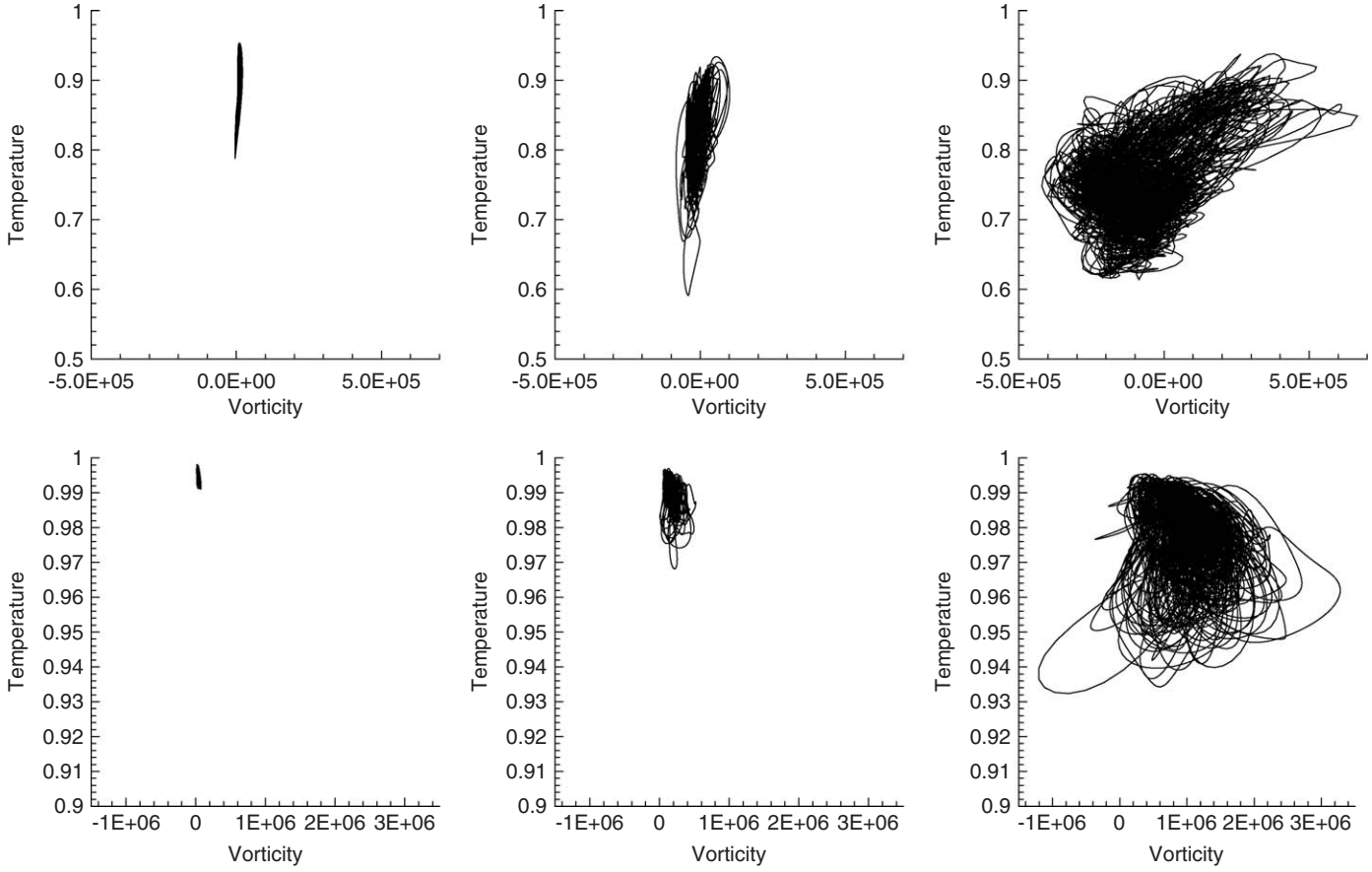

Fig. 9. Temperature–vorticity time series phase portraits for $Ra = 10^7$ (left), $Ra = 10^8$ (middle) and $Ra = 10^9$ (right). Temperature and vorticity at locations A = (0.0011, 3.5) and B = (0.0301, 3.5) are presented in the bottom and top rows, respectively.

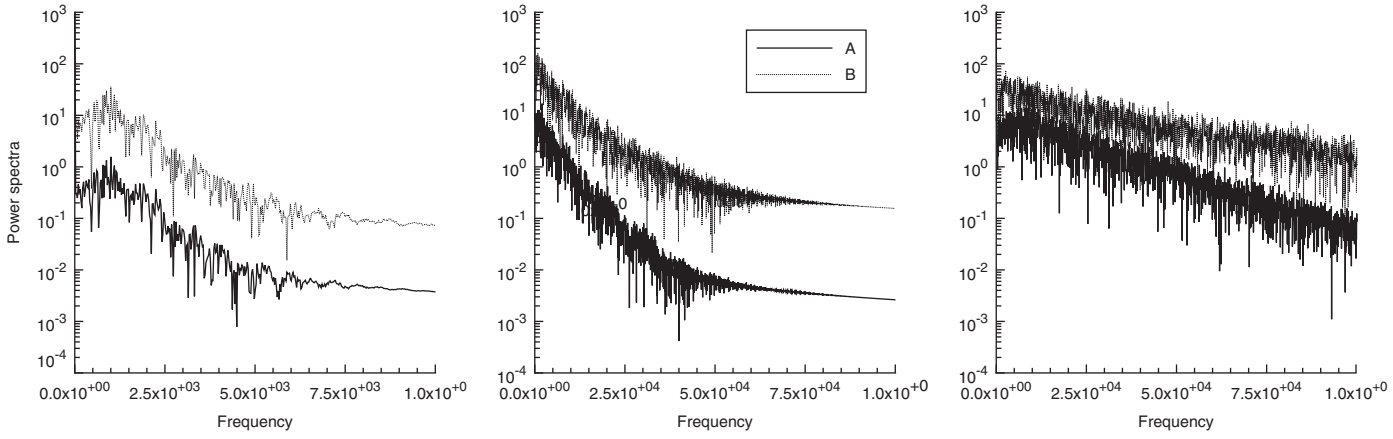

Fig. 10. Power spectra of temperature time series at locations A = (0.0011, 3.5) and B = (0.0301, 3.5) for $Ra = 10^7$ (left), $Ra = 10^8$ (middle) and $Ra = 10^9$ (right).

On the contrary, the maxima of turbulent heat fluxes and temperature variance are located in the boundary layers.

6. Conclusions

The velocity-vorticity formulation of LES in combination with the wavelet transform based BEM presented in this paper shows good potential for solving turbulent fluid flow problems with the LES approach. Solution of boundary vorticity values with wavelet based BEM provides boundary conditions for the transport equations, which we are solving by FEM. Using the wavelet transform with the BEM enabled us to use meshes with $\approx 10^5$ nodes. Higher mesh densities will be possible in the near future, as well as the extension of the code to 3D, by the use of domain decomposition and parallel computing.

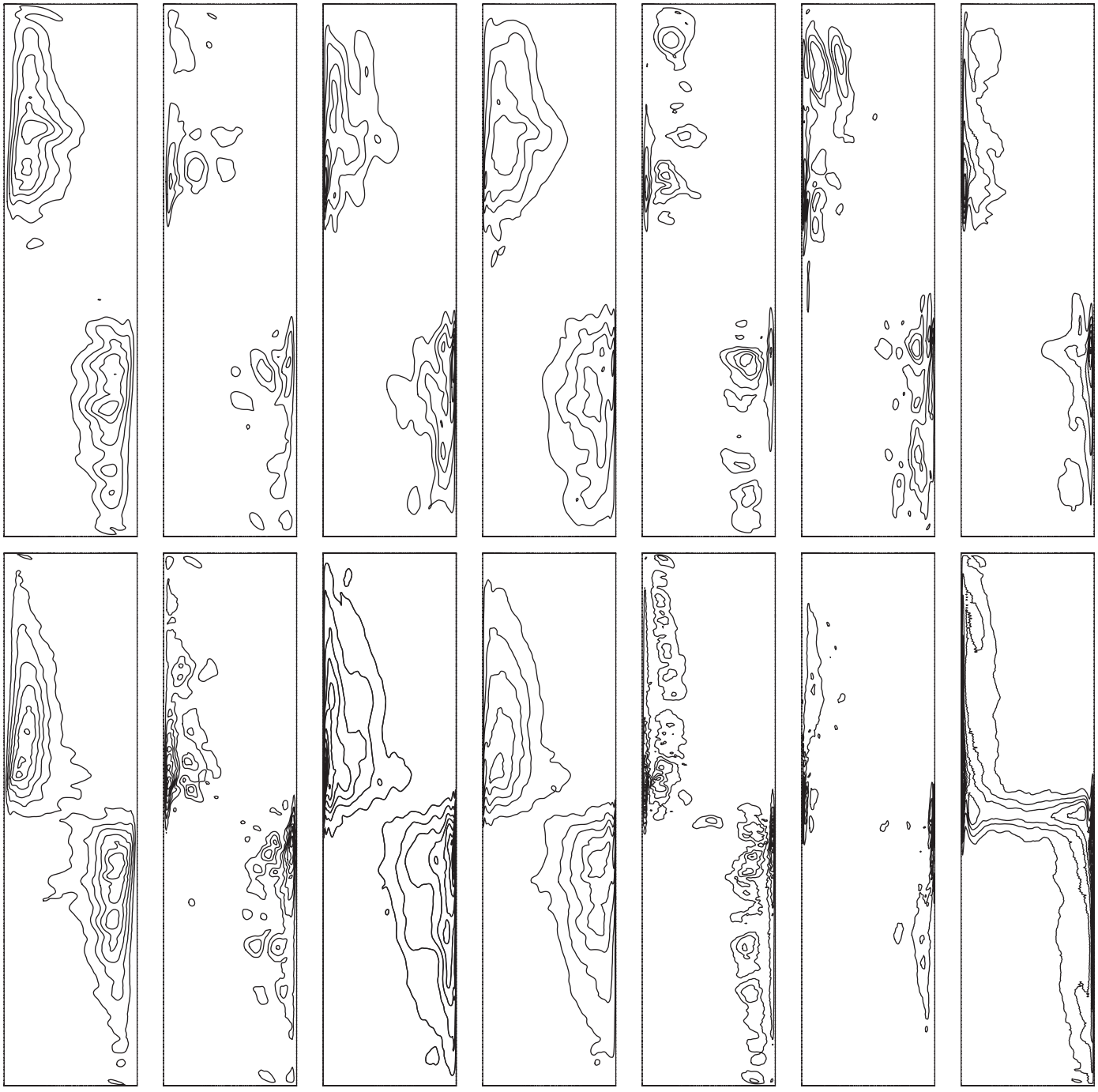

Fig. 11. Turbulence statistics for $Ra = 10^8$ (top row) and $Ra = 10^9$ (bottom row). Left to right: Reynolds stresses $\overline{v'_x v'_x}$, $\overline{v'_x v'_y}$, $\overline{v'_y v'_y}$, turbulent kinetic energy $k = \frac{1}{2}\overline{v'_i v'_i}$, turbulent heat fluxes $\overline{v'_x T'}$, $\overline{v'_y T}$ and temperature variance $\overline{T'T'}$.

Unsteady natural convection in a 1:4 differentially heated enclosure was investigated using LES for enclosure width based Rayleigh number between $Ra = 10^7$–10^9. The flow was oscillatory at $Ra = 10^7$, while for higher Rayleigh number values it became increasingly irregular, non-repeating and chaotic. The transition to turbulent flow was investigated by studying time series plots, power spectra and vorticity–temperature phase diagrams. Turbulence statistics were calculated to confirm that for $Ra > 10^8$ downstream in the vertical boundary layers the flow is turbulent, while the flow upstream of vertical boundary layers remains laminar. Heat transfer was characterized with the average Nusselt number, its time series and its relation to the Rayleigh number. The results of damped LES simulations were found in excellent agreement with the benchmark DNS results of Xin and Le Quéré [9]. On the other hand, the LES without damping simulation underestimated the heat transfer severely. Comparing Piomelli and Van Driest damped LES we found that both datasets were qualitatively equal; the Van Driest simulation

yielding the average Nusselt number slightly closer to the benchmark.

Acknowledgements

The first author gratefully acknowledges the support of the Institute of Fluid Mechanics and Hydraulic Machinery and HLRS of the University of Stuttgart in the framework of the EC-funded HPC-Europa project under Contract no. 506079.

References

[1] Davies G, Jones I. Natural convection of air in a square cavity: a bench mark numerical solution. Int J Numer Methods Fluids 1983;3:249–64.
[2] Vierendeels J, Merci B, Dick E. Numerical study of the natural convection heat transfer with large temperature differences. Int J Numer Methods Heat Fluid Flow 2001;11:329–41.
[3] Vierendeels J, Merci B, Dick E. A multigrid method for natural convective heat transfer with large temperature differences. Int J Comput Appl Math 2004;168:509–17.
[4] Škerget L, Samec N. BEM for the two-dimensional plane compressible fluid dynamics. Eng Anal Bound Elem 2005;29:41–57.
[5] Weisman C, Calsyn L, Dubois C, Quéré PL. Sur la nature de la transition a l'instationare d'un ecoulement de convection naturelle en cavite differentiellement chauffee a grands ecarts de temperature, Comptes rendus de l'academie des sciences Serie II b. Mecanique; 2001. p. 343–50.
[6] Oosthuizen PH, Paul JT. Natural convection in a rectangular enclosure with two heated sections on the lower surface. J Comput Phys 2005;26:587–96.
[7] Ingber MS. A vorticity method for the solution of natural convection flows in enclosures. Int J Numer Methods Heat Fluid Flow 2003;13:655–71.
[8] Hsieh KJ, Lien FS. Numerical modeling of buoyancy-driven turbulent flows in enclosures. Int J Heat Fluid Flow 2004;25(4): 659–70.
[9] Xin S, Quéré PL. Direct numerical simulations of two-dimensional chaotic natural convection in a differentially heated cavity of aspect ratio 4. J Fluid Mech 1995;304:87–118.
[10] Salat J, Xin S, Joubert P, Sergent A, Penot F, Quéré PL. Experimental and numerical investigation of turbulent natural convection in a large air-filled cavity. Int J Heat Fluid Flow 2004;25: 824–32.
[11] Peng SH, Davidson L. Large eddy simulation for turbulent bouyant flow in a confined cavity. Int J Heat Fluid Flow 2001;22:323–31.
[12] Tenaud C, Pellerin S, Dulieu A, Phuoc LT. Large eddy simulation of a spatially developing incompressible 3D mixing layer using $v-\omega$ formulation. Comput Fluids 2005;34:67–96.
[13] Mansfield JR, Knio OM, Meneveau C. A dynamic LES scheme for vorticity transport equation: formulation and a priori tests. J Comput Phys 1998;145:693–730.
[14] Škerget L, Hriberšek M, Kuhn G. Computational fluid dynamics by boundary domain integral method. Int J Numer Methods Eng 1999; 46:1291–311.
[15] Ramšak M, Škerget L. A subdomain boundary element method for high-Reynolds laminar flow using stream function—vorticity formulation. Int J Numer Methods Fluids 2004;46:815–47.
[16] Žunič Z, Škerget L, Hriberšek M, Ravnik J. Boundary element-finite element method for velocity-vorticity formulation of Navier–Stokes equations. In: WIT transactions on modelling and simulation, vol. 41; 2005. p. 793–802.
[17] Ravnik J, Škerget L, Hriberšek M. The wavelet transform for BEM computational fluid dynamics. Eng Anal Bound Elem 2004;28: 1303–14.
[18] Pope S. Turbulent flows. Cambridge: Cambridge University Press; 2000.
[19] Sagaut P. Large eddy simulation for incompressible flows, an introduction. Berlin: Springer; 2002.
[20] Taylor GI. The transport of vorticity and heat through fluids in turbulent motion. Proc London Math Soc Ser A 1932;151–421.
[21] Smagorinsky J. General circulation experiments with the primitive equations: I. The basic equations. Mon Weather Rev 1963;91:99–164.
[22] Mansour NN, Ferziger JH, Reynolds WC. Large-eddy simulation of a turbulent mixing layer. Report TF-11, Thermosciences Division, Department of Mechanical Engineering, Standford University; 1978.
[23] Winckelmans GS, Lund TS, Carati D, Wray AA. A priori testing of subgrid-scale models for the velocity pressure and vorticity-velocity formulations. Proceedings of the summer program 1996, Center for Turbulence Research; 1996.
[24] Breuer M. Direkte Numerische simulation und large-eddy simulation turbulenter Strömungen auf Hochleistungsrechnern. Aachen: Shaker Verlag; 2002.
[25] Wrobel LC. The boundary element method. New York: Wiley; 2002.
[26] Škerget L, Hriberšek M, Žunič Z. Natural convection flows in complex cavities by BEM. Int J Numer Methods Heat Fluid Flow 2003;13:720–35.
[27] Beylkin G, Coifman R, Rokhlin V. Fast wavelet transforms and numerical algorithms. Commun Pure Appl Math 1991;44:141–83.
[28] Sleijpen GLG, Fokkema DR. Bicgstab(l) for linear equations involving unsymmetric matrices with complex spectrum. El Trans Numer Anal 1993;1:11–32.
[29] Ghia U, Ghia K, Shin C. High-*Re* solutions for incompressible flow using the Navier–Stokes equations and a multigrid method. J Comput Phys 1982;48:387–411.
[30] Horvat A. Modeliranje turbulentne naravne konvekcije v kapljevini z notranjo generacijo toplote z metodo velikih vrtincev. PhD thesis, University of Ljubljana, Faculty for Mathematics and Physics; 2001.
[31] Tian YS, Karayiannis TG. Low turbulence natural convection in an air filled square cavity: Part I: the thermal and fluid flow fields. Int J Heat Mass Transfer 2000;43:849–66.
[32] Decker W. Numerical studies of bifurcations and chaos in natural convection. PhD thesis, University of Virgina, USA; 1996.